NANO LETTERS
Letter
pubs.acs.org/NanoLett

Jointly Tuned Plasmonic–Excitonic Photovoltaics Using Nanoshells

Daniel Paz-Soldan,[†] Anna Lee,[†] Susanna M. Thon,[†] Michael M. Adachi,[†] Haopeng Dong,[†,‡] Pouya Maraghechi,[†] Mingjian Yuan,[†] André J. Labelle,[†] Sjoerd Hoogland,[†] Kun Liu,[§] Eugenia Kumacheva,[§] and Edward H. Sargent*[,†]

[†]Department of Electrical and Computer Engineering, University of Toronto, 10 King's College Road, Toronto, Ontario, M5S 3G4, Canada

[‡]Department of Chemistry, Tsinghua University, Beijing 100084, P. R. China

[§]Department of Chemistry, University of Toronto, 80 Saint George Street, Toronto, Ontario, M5S 3H6, Canada

Supporting Information

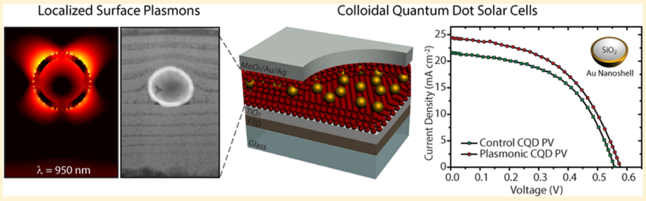

ABSTRACT: Recent advances in spectrally tuned, solution-processed plasmonic nanoparticles have provided unprecedented control over light's propagation and absorption via engineering at the nanoscale. Simultaneous parallel progress in colloidal quantum dot photovoltaics offers the potential for low-cost, large-area solar power; however, these devices suffer from poor quantum efficiency in the more weakly absorbed infrared portion of the sun's spectrum. Here, we report a plasmonic–excitonic solar cell that combines two classes of solution-processed infrared materials that we tune jointly. We show through experiment and theory that a plasmonic–excitonic design using gold nanoshells with optimized single particle scattering-to-absorption cross-section ratios leads to a strong enhancement in near-field absorption and a resultant 35% enhancement in photocurrent in the performance-limiting near-infrared spectral region.

KEYWORDS: *Colloidal quantum dots, nanoshells, localized surface plasmons, near-field, photovoltaics*

Plasmonic enhancements to absorption in semiconductors and organic molecules are achieved via near-field effects,[1−5] path-length increases via far-field scattering,[6−8] and surface plasmon polariton (SPP) waveguiding.[9−11] Plasmonic light management has been applied to optoelectronic devices such as lasers,[12] light emitters,[13] photodetectors,[14] biosensors,[15] and solar cells.[16,17] Prior efforts to utilize plasmonic enhancements in solar cells have been aimed primarily at better visible-wavelength enhancements, achieved mostly via improved in-coupling.[18] The visible-wavelength emphasis derives from the fundamental surface plasmon resonances of silver or gold.[4,5,19]

In fact, half of the sun's power reaching the earth lies in the infrared. It is in better harvesting photons in this spectral regime that colloidal quantum dot (CQD) photovoltaics offer an attractive advantage over many organic and inorganic solar technologies. Nevertheless, while they have advanced rapidly, CQD photovoltaics remain limited by their incomplete absorption of light in the infrared.

We took the view that localized surface plasmon resonance (LSPR) engineering could provide an appreciable enhancement in CQD photovoltaic performance. A near-field enhancement of the photocarrier generation rate, in the vicinity of the plasmonic nanoparticles, would be particularly advantageous in this class of thin film devices.

Embedding the plasmonic enhancers directly into the quantum dot absorber film would be necessary to achieve the intended near-field enhancement. It would also require surmounting a number of key challenges. First, a potential source of loss in plasmonic solar cells is parasitic absorption in the metal that subtracts from the photovoltaic device photocurrent.[20] The beneficial field enhancement due to the plasmonic particle must exceed the punitive absorption in the plasmonic enhancer for a net benefit to be realized. The scattering-to-absorption ratio, $S = \sigma_{\mathrm{scat}}/\sigma_{\mathrm{abs}}$, in which the numerator takes into account both near-field and far-field scattering by the plasmonic particle, must desirably meet the condition $S \gg 1$. A second consideration is that mixing plasmonic particles with quantum dots in the solution state results in film variability, leading to irreproducibility in optical and electronic properties. Therefore, to maximize the fidelity of the results, a controlled drop-casting method was required for the plasmonic nanoparticles (see Methods). Lastly, metal nanoparticles can act as recombination centers in photovoltaic films, leading to losses that would, if not properly managed, offset any current gains due to enhanced absorption. A thin insulating shell on the metal nanoparticles is necessary to reduce this effect;[1,21] however, it should be noted that a thicker dielectric shell makes the field less dispersive, leading to reduced interaction volume with the near field.[19] Therefore, appropriate surface passivation requires a careful balance between ensuring colloidal chemical stability for solution

Received: December 13, 2012
Revised: February 15, 2013
Published: February 27, 2013

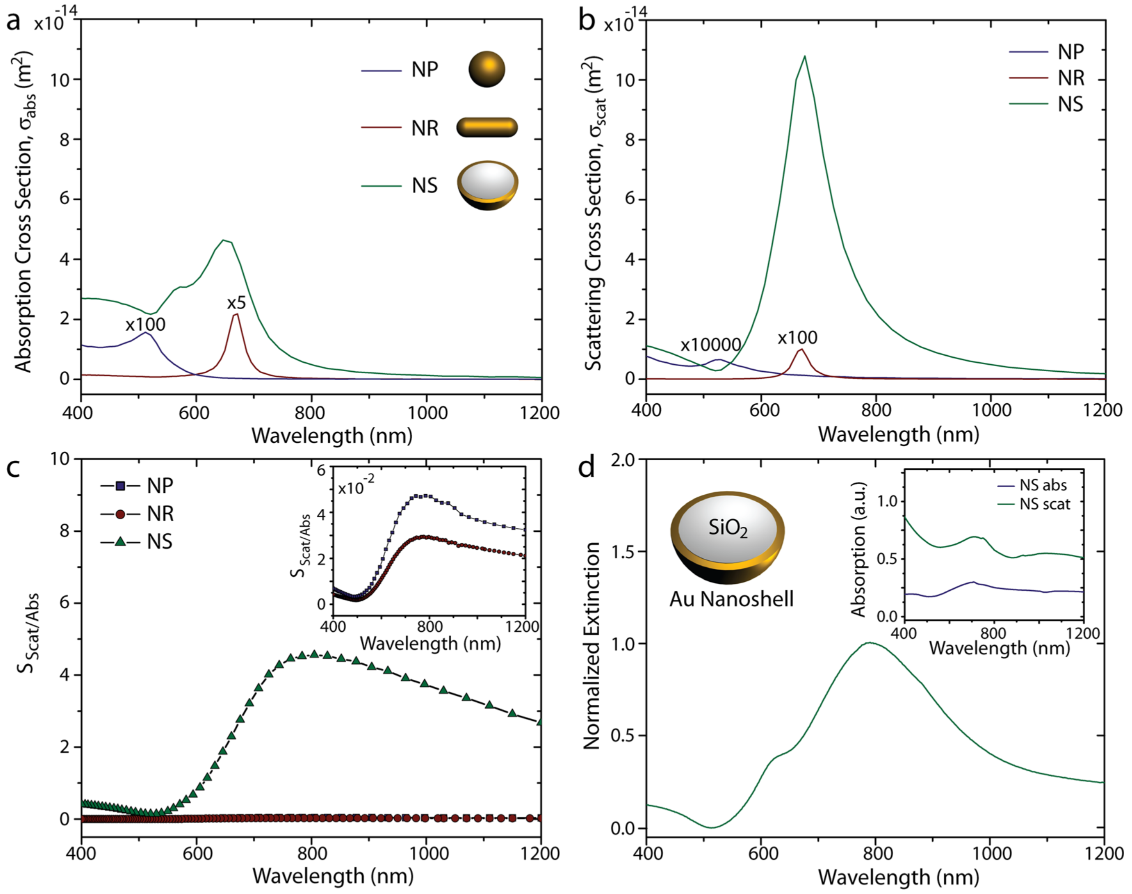

Figure 1. Absorption (a) and scattering (b) cross-section spectra as a function of particle size and shape. The scattering cross sections take into account both near- and far-field effects. Spherical nanoparticles (NP, diameter = 20 nm) have a limited response beyond $\lambda = 600$ nm, while nanorods (NR, diameter = 10 nm, length = 40 nm) and nanoshells (NS, core diameter = 120 nm, shell thickness = 15 nm) have tunable localized surface plasmon resonances (LSPRs) in the infrared wavelength region. A medium of index 1 was used. The nanoparticle and nanorod spectra are scaled as noted next to the curves for visual clarity. (c) Calculated scattering-to-absorption ratios (S) showing that nanorods and nanoparticles of commonly synthesized sizes are absorptive while nanoshells have broadband external field enhancement which exceeds parasitic absorption. The inset shows the same data for nanorods and nanoparticles on a smaller scale. (d) Experimental extinction spectrum of nanoshells in a methanol solution. Insets: schematic of a gold nanoshell cross-section (left) and measured scattering and absorption of nanoshell films (right).

processing, electronic insulation from surface recombination, and local optical enhancement.

We employed full-wave finite-difference time-domain (FDTD) simulations to evaluate the potential impact of incorporating different types of metal nanoparticles into excitonically tuned solar cells. Our criteria for candidate particles were as follows: (1) compatibility with solution processing; (2) size range of less than ~150 nm for integration in films with thicknesses of less than ~400 nm; (3) LSPRs tunable to the near-infrared (NIR) portion of the solar spectrum; and (4) scattering-to-absorption ratios (S) of greater than 1. Although silver particles are known to be strong scatterers,[22,23] the first three criteria led us to focus on gold particles which have resonances that are more easily tunable to the NIR.

Figure 1 shows the simulated absorption and scattering cross sections and the S values for several different types of gold nanoparticles. The dipole resonance of spherical nanoparticles can be tuned in the visible range as a function of the particle radius. At diameters greater than 150 nm, broadband multipole modes arise in the NIR spectral range, but these generally exhibit lower LSPR amplitudes.[24] A second candidate for infrared-tunable plasmonic particles is gold nanorods.[25,26] These exhibit two spectrally separated LSPRs due to the coherent oscillation of the conduction band electrons along each of the particle axes (transverse and longitudinal), and the longitudinal plasmon can be spectrally tuned through the NIR by varying the aspect ratio.[27,28] However, typically synthesized nanorods exhibit a strong electric field within the metal, resulting in a S of much less than 1 over all wavelengths of interest. A similar phenomenon is found for easily synthesized spherical nanoparticles (Figure 1c).

The failure of conventional plasmonic particles to meet the needs of excitonically tuned photovoltaics motivated us to investigate spherical dielectric–metal core–shell nanoparticles, also known as nanoshells.[29,30] Figure 1d shows the measured extinction spectrum of nanoshells in methanol solution with a LSPR centered at 800 nm with a full-width at half-maximum of 280 nm. We find that the extinction (absorption + near- and far-field scattering) cross-section is 3–5 orders of magnitude larger than that of either spherical nanoparticles or nanorods (Figure 1a,b). Due to the presence of a thin metallic shell (~15 nm), we expect that the optical interaction volume of these particles is therefore much larger, reducing the areal density required to scatter incident light completely while minimizing absorption. The theoretical S factor reaches its maximum at 4.5

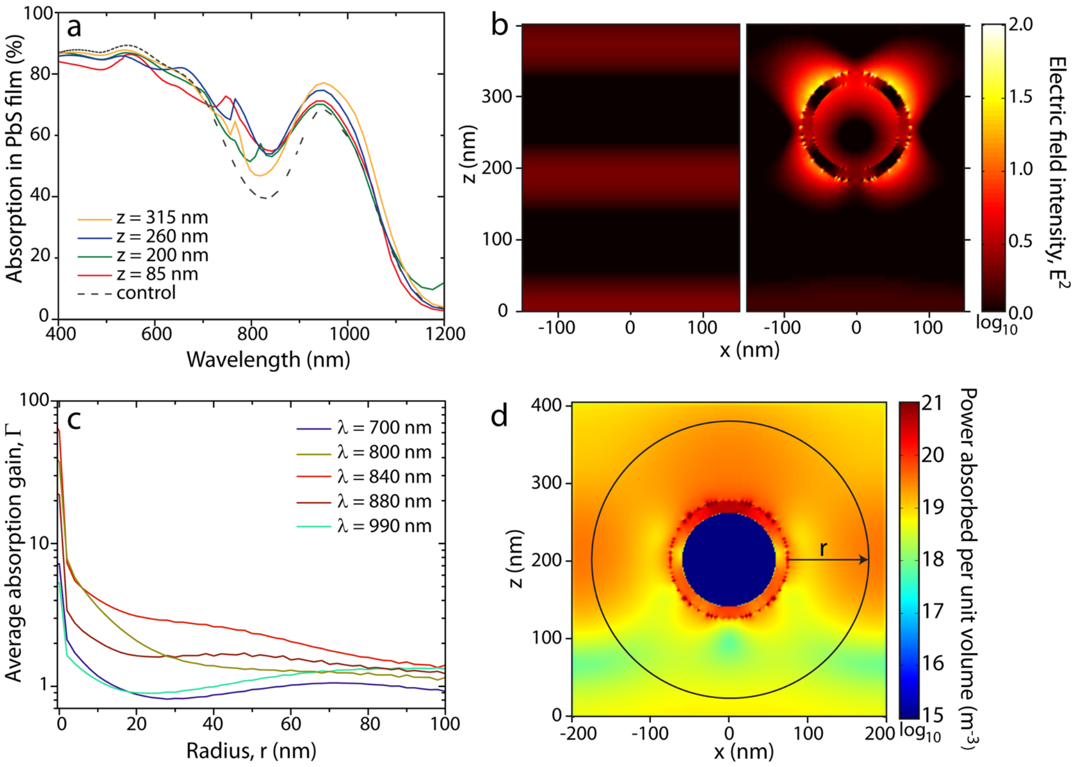

Figure 2. 3D FDTD simulation of plasmonic−excitonic films. (a) Absorption spectra (including back-reflector) in a 400 nm thick PbS quantum dot film with nanoshells embedded at different values of z, the distance from the PbS bottom-illuminated interface to the center of the nanoshells. The nanoshells are periodically spaced by an average of 300 nm. The Supporting Information (Figure S7) contains the results for several different periodic spacings which indicate that the qualitative spectral shapes and intensities are independent of simulated period. The maximum integrated current is found to occur when the nanoshell is at a z position of 260 nm. (b) Electric field intensity (E^2) profiles in the control film (left) and plasmonic film (right) on a log scale at the CQD exciton wavelength, λ = 950 nm. (c) Average absorption gain, Γ, the ratio of absorption in the nanoshell-embedded PbS film to the unenhanced PbS film, as a function of radial distance, r, from the edge of the nanoshell plotted for a range of wavelengths around the LSPR. (d) Absorption profile (log scale) at λ = 840 nm of a nanoshell embedded in a PbS CQD film demonstrating the strong electromagnetic near-field in the vicinity of the nanoshell. Power absorbed per unit volume is in units of m^{-3} (absorbed power per unit volume is normalized to the source power).

and is larger than 3 over a wide spectral range in the near-infrared region (Figure 1c). Additional calculations for large nanorods (66 nm in diameter and 512 nm in length), spherical nanoparticles (150 nm in diameter), and spherical dielectric particles (150 nm in diameter) (Supporting Information, Figure S6) show that gold nanorods and nanospheres require sizes greater than 150 nm in at least one dimension to achieve S values comparable to the nanoshells at the wavelengths of interest. This makes the rods and spheres difficult to incorporate into thin film CQD devices. In sum, the nanoshells offer superior scattering cross sections at the near-infrared wavelengths of interest compared to other structures with comparable volumes.

We sought to verify that $S > 1$ for nanoshells by experimentally measuring the relative scattering and absorption contributions. We deposited a thin layer of nanoshells by drop-casting from the solution phase onto a glass slide and separated the absorption and scattering components using integrating sphere spectrophotometry (see Methods). Figure 1d inset shows that, in the solid state, S is at least 2 over all wavelengths of interest (400−1200 nm). In contrast, the S of nanorods deposited by a similar method was measured to be much less than 1 over the same wavelength range (Supporting Information, Figure S1). We conclude from these studies that the scattering component is the major contribution from the measured extinction of nanoshells shown in Figure 1d; that is, they are less absorptive and thus meet all of the criteria outlined above for incorporation into excitonic solar cells.

Next, we investigated the effects of incorporating gold nanoshells into thin-film photovoltaic devices. CQDs offer wide-ranging bandgap tunability through the quantum size effect, and solar cells based on this material have recently reached a certified record power conversion efficiency of 7%.[31] The absorption spectrum of this material exhibits a peak at the excitonic transition; however, light in the NIR spectral region (700−1000 nm) is not fully absorbed in films of thickness ~400 nm, the transport length (sum of the minority carrier diffusion length and the width of the depletion region at the maximum power) of today's best photovoltaic CQD films. Past strategies for overcoming this absorption−extraction compromise include interpenetrating the acceptor material and the CQD film to increase the width of the depletion region using TiO_2 nanostructures,[32] a concept analogous to bulk heterojunction cells in organic photovoltaics.[33] Nevertheless, planar cells having an area-minimizing charge-separating electrode have to date offered the best performance. Plasmonic enhancements would address the present-day absorption-extraction trade-off problem by increasing light absorption for a given quantum dot film volume and for a given planar charge-separating interfacial area.

In Figure 2 we use FDTD simulations to explore the optical properties of gold nanoshells embedded within PbS CQD films.

Figure 2a–b shows the relative enhancements expected from an array of nanoshells at various vertical locations, *z*, within the CQD film. Placing them near the illuminated side of the film leads to significant parasitic absorption in the visible spectral range (400–600 nm), limiting the optical enhancement. Moving the nanoshells toward the rear gold reflector allowed for effective scattering of weakly absorbed infrared radiation while minimizing the impact on short-wavelength light. Placing the nanoshell too close to the back of the device, near the reflector, reduced the volume of CQD material which interacted with the enhanced near-field. We predicted from quantitative simulations that the optimal enhancement would occur when nanoshells were placed approximately two-thirds of the way into the CQD film as measured from the illuminated interface (Supporting Information, Figure S2). We emphasize that, in our simulations, the relatively large-diameter nanoshells displaced the equivalent volume of CQDs, indicating that the plasmonic effect more than overcame the loss of absorbing PbS volume.

Next, we calculate the relative contribution of the observed absorption enhancement attributable to the field enhancement. In Figure 2c–d we embed the nanoshells in a film of CQD absorber material and calculate the average absorption gain, Γ, which we define as the power absorbed in the nanoshell case normalized by the absorption in the film without nanoshells. We plot Γ as a function of radial distance, *r*, from the center of the nanoshell for different wavelengths and observe a significant absorption enhancement in the surrounding PbS film (Figure 2b). The absorption gain is largest for wavelengths near $\lambda = 840$ nm and decays quickly from the nanoshell surface, remaining greater than 1 for a range of wavelengths near the plasmonic resonance out to 100 nm from the nanoparticle. This indicates that resonant near-field enhancement is the primary mechanism contributing to enhanced absorption with a small additional contribution from enhanced far-field scattering into the optical modes of the device.

Using the insights gained from the set of simulations summarized in Figure 2, we designed a solution-processed plasmonic CQD solar cell employing gold nanoshells. Nanoshells consisting of an inner core radius of 60 nm (SiO_2) and outer shell thickness of 15 nm (Au) are capped with polyvinylpyrrolidone (PVP)[34,35] and show a broad LSPR at 800 nm in methanol solution (Figure 1d), a solvent chemically compatible with our CQD films. Our solar cells employed the depleted heterojunction architecture,[36] and the quantum dot film was formed on top of a TiO_2 electrode using a layer-by-layer process (see Methods). We deposited the nanoshell solution by drop-casting and drying under low vacuum after two-thirds of the total CQD material had been deposited (see Methods). The finished device consisted of the remaining third of the CQD layers and an evaporated ohmic contact consisting of MoO_3/Au/Ag.

Figure 3a shows a schematic representation of our plasmonic CQD solar cell design. We use 980 nm bandgap PbS CQDs and a TiO_2 electron acceptor. Figure 3b shows a top-view low-magnification SEM image, leading us to an estimated average surface coverage of approximately 10 nanoshells per square micrometer. The average nanoshell areal density was chosen to provide full optical coverage based on the peak scattering cross-section of approximately 10^{-13} m^2 while minimizing inter-particle coupling effects due to undesired aggregation. Figure 3c shows a cross-sectional TEM image of a sample prepared via focused ion beam milling of the constituent layers. Energy dispersive X-ray analysis confirms the atomic composition of nanoshells embedded in CQD layers (Supporting Information, Figure S5). Also visible are the individual spin-cast CQD layers which surround and embed the gold nanoparticle.

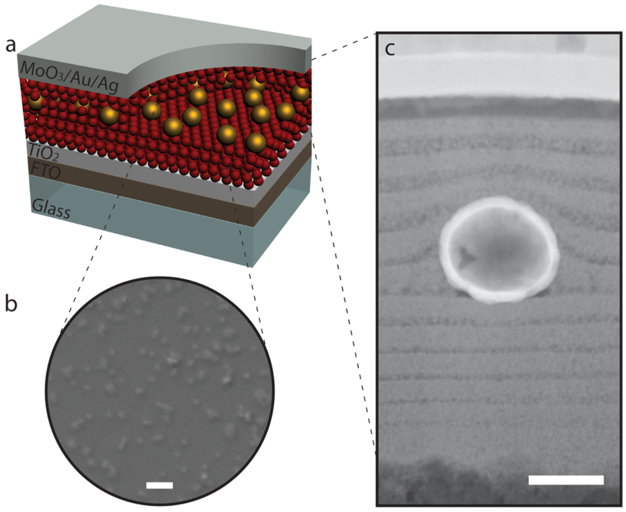

Figure 3. Plasmonic–excitonic solar cell device design. (a) Schematic of the PbS CQD depleted heterojunction device with embedded nanoshells. (b) Top view scanning electron micrograph (SEM) showing representative density of nanoshells after CQD deposition. Scale bar, 1 μm. (c) Cross-sectional transmission electron micrograph (TEM) showing a single gold nanoshell embedded in a PbS CQD film. Scale bar, 100 nm.

The absorption spectra in a single pass through the CQD films were measured using integrating sphere spectrophotometry. The spectra of two representative samples with and without nanoshells are shown in Figure 4a. By subtracting the absorption curves of a nanoshell-embedded CQD film and a bare CQD film as a control, we observe a broadband absorption enhancement as high as 100%, centered near the plasmonic LSPR at 820 nm (Figure 4b). This absorption enhancement is primarily attributed to the near-field scattering from nanoshells and also includes contributions from absorption in the nanoshells themselves and far-field scattering. The resonance is red-shifted by approximately 20 nm relative to that measured in solution due to the higher index of the surrounding medium ($n_{CQD} \sim 2.6$). Enhancements at wavelengths above 1000 nm are expected to originate from enhanced absorption in the substrate and gold top contact due to multiple scattering. If we consider the high scattering-to-absorption ratio of nanoshells, we expect most of the measured absorption enhancement at wavelengths shorter than the CQD film bandgap to originate from absorption in the quantum dot film and not from parasitic absorption in the nanoshells, as supported by simulations (Figure 2).

The performance of plasmonic CQD devices with nanoshells incorporated was evaluated in solar cell devices measured under simulated AM 1.5 solar illumination (see Methods). Figure 4b shows current–voltage curves of the higher-performing devices. We measured an overall power conversion efficiency (PCE) enhancement of 11% over a nonplasmonic device (PCE = 6.9% vs 6.2% for the control). The enhancement in performance is primarily due to the 13% enhancement in short circuit current density, J_{SC} (24.5 mA cm^{-2} vs 21.6 mA cm^{-2} for the control), while there is no statistically significant enhancement or degradation of the open circuit voltage, V_{OC}, or fill factor, FF

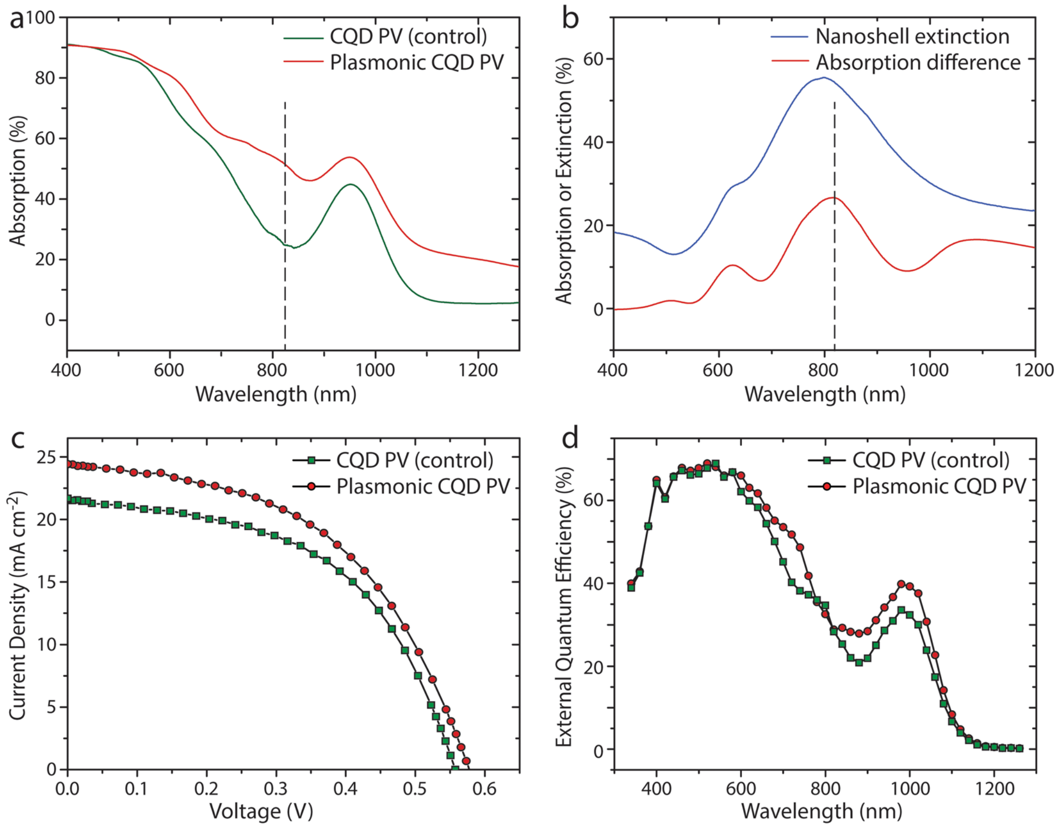

Figure 4. Performance of plasmonic CQD photovoltaics. (a) Single-pass absorption spectra of representative CQD films with and without embedded nanoshells. (b) The absorption enhancement exhibits a peak near 820 nm and closely matches the nanoshell extinction spectrum, suggesting that a resonant effect accounts for the observed enhancement. (c) Measured current−voltage characteristics under AM1.5 simulated solar illumination for representative control and plasmonic devices. J_{sc} enhancement of 13% and PCE enhancement of 11% were observed in the plasmonic device. (d) External quantum efficiency spectra of control and plasmonic CQD solar cells. A peak 35% enhancement centered at a wavelength of 880 nm was observed in the plasmonic device.

(Table S1). This trend indicates that we were able to maintain the fidelity of our thin films, overcome any added recombination effects resulting from nanoshell integration, and simultaneously enhance the density of photogenerated carriers by enhancing the CQD film absorption.

To test the hypothesis that the performance enhancement was due to rational control of the properties of the plasmonic−excitonic solar cell, we also fabricated a series of negative control devices using highly absorptive nanorods. We adjusted the concentration of the deposited nanorod solution to match the measured peak extinction of the optimized nanoshell solution to within 20% to operate in a comparable optical coverage regime. The results are summarized in Table S2 and show no significant change in device current for the nanorod devices compared to the controls. These results indicate that plasmonic−excitonic solar cells must follow strict design criteria such as those outlined previously to benefit from plasmonic enhancements.

We employ external quantum efficiency (EQE) measurements to analyze in greater detail the origins of enhanced photocurrent in plasmonic CQD solar cells. The results of EQE measurements of two representative samples are shown in Figure 4c. We observe a strong spectral correlation between the enhanced absorption shown in Figure 4a and the enhanced quantum efficiency. The peak EQE enhancement of approximately 35% occurs at a wavelength near 880 nm, which falls within the full-width at half-maximum of the nanoshell LSPR and is very close to the wavelength of peak absorption enhancement suggesting a resonant near-field effect due to the plasmonic nanoshells. Previous studies have predicted that the peak wavelength for near-field measures of gold plasmonic particle resonances should be red-shifted compared to the far-field and absorption peak wavelengths,[37] which is consistent with the possibility that most of the device EQE enhancement is attributable to plasmonic near-field effects.

We used our plasmonic and control EQE spectra and the internal quantum efficiency (IQE) spectrum for the control device (calculated by dividing the EQE spectrum by the double-pass absorption spectrum) to quantify the relative contributions of enhanced absorption in the CQD film and absorption in the nanoshells to the absorption difference spectrum shown in Figure 4b. The enhanced absorption in the CQD film due to the presence of the nanoshells is given by the EQE difference spectrum divided by the IQE spectrum, and the parasitic absorption in the nanoshells is given by the difference between this value and the difference in the absorption spectra. Integrating over all wavelengths, we determined that 54% of the enhanced absorption occurred in the CQD film and 46% of the enhanced absorption occurred in the nanoshells, verifying our assertion that S for the nanoshells is slightly greater than one. We note that the EQE difference spectrum is zero or positive across all wavelengths, indicating that the presence of parasitic absorption in the nanoshells did not detract from device performance at any photon energy.

Plasmonic control of light on the nanoscale has shown wide applicability to subwavelength-scale sensing and imaging enhancements.[12−15] In this work, we demonstrated a new use for these types of effects: spectrally matched infrared enhancement in all-solution-processed thin film plasmonic-excitonic solar cells. We took advantage of the subwavelength near-field scattering effects of colloidal plasmonic nanoparticles to increase effective absorption lengths for NIR photons to length scales much larger than the absorbing film thickness. Given the mismatch in optical absorption lengths and carrier extraction lengths, creative solutions to the absorption−extraction compromise will continue to be critical to achieving high efficiencies in excitonic photovoltaics. The optical and electrical design considerations outlined here will direct strategies to maximize the plasmonic effect for improving the performance of future thin-film optoelectronic devices.

Methods. *Colloidal Quantum Dot Synthesis.* PbS quantum dots were synthesized according to a previously published method,[38] followed by a solution-phase metal halide ($CdCl_2$) treatment.[31] 1.0 mL of metal halide precursor ($CdCl_2$ and tetradecylphosphonic acid (TDPA) dissolved in oleylamine with 13.6:1 Cd:TDPA molar ratio) was introduced into the reaction flask after sulfur source injection during the slow cooling process. The PbS CQDs were isolated by the addition of 60 mL of acetone followed by centrifugation after the reaction temperature reached 30−35 °C. The nanocrystals were then purified by dispersion in toluene and reprecipitation with acetone/methanol (1:1 volume ratio) and redissolved in anhydrous toluene. The solution was washed with methanol three times with the final redispersion in octane at 50 mg mL^{-1}.

Finite-Difference Time-Domain Simulations. Finite-difference time-domain (FDTD) simulations were carried out using software package Lumerical FDTD solutions version 8 (http://www.lumerical.com). Scattering and absorption crosssections were determined following the Mie scattering method. A total-field scattered-field (TFSF) source surrounds the particle of interest. A broadband (λ = 400−1200 nm) source, polarized along the cylinder axis, was injected. The region is surrounded by perfectly matched layers (PMLs) which absorb most incident radiation over a wide range of angles. Two analysis groups, one inside the source boundary (measuring total field) and one outside the source boundary (measuring scattered field), calculate the optical cross sections. In Figure 2, the simulated structure is a PbS-CQD effective medium (400 nm)/MoO3 (50 nm)/Au (150 nm) with and without embedded Au nanoshell, and the absorption was integrated within the PbS material only. The background index of refraction is matched to that of the PbS material to remove interference fringes in the absorption spectra.

Plasmonic−Excitonic Solar Cell Fabrication. PbS CQD photovoltaic devices were fabricated on cleaned FTO-coated glass substrates (Pilkington, TEC 15). The n-type ZnO/TiO_2 electrode was made from a colloidal ZnO nanoparticle solution (Alfa Aesar Nanoshield ZN-2000) diluted to 25% in DI H_2O. FTO substrates were coated by spin-casting at 2000 r.p.m. and treated with a 120 mM TiCl4 solution at 70 °C for 30 min. The substrates were then rinsed with deionized water and annealed on a hot plate at 520 °C for 45 min in air ambient. A layer-by-layer spin-casting process was used to build up the CQD film. Under an ambient atmosphere, two drops of PbS CQD were dropped through a 0.22 μm filter on the ZnO/TiO_2 substrate and spin-cast at 2500 r.p.m. A solid-state ligand exchange with mercaptopropionic acid (MPA) was done by flooding the surface for 3 s, then spin-casting dry at 2500 r.p.m. Finally two washes with MeOH were used to remove unbound ligands. In the case of plasmonic particle deposition, nanorods were synthesized based on the seed-mediated growth method,[26,39] and nanoshells were purchased from NanoComposix, Inc. Nanoshells in methanol solution were centrifuged at 1000 r.p.m. for 15 min, and the centrifugation cycle was repeated twice. The final concentration of nanoshells dissolved in methanol was 30 mg mL^{-1} and sonicated for 40 s (42 ± 3 kHz) and used immediately. Nanoshell solution (35 μL) was deposited on the PbS film on a level surface in a circular reservoir and allowed to dry under low vacuum (~10^{-3} Torr) for 60 s. Nanoshell deposition was done after 8 PbS layers and was followed by four additional PbS layers. Each device (control and plasmonic) consisted of 12 total PbS layers. Top electrode deposition consisted of 10 nm thermally evaporated molybdenum trioxide deposited at a rate of 0.2 Å s^{-1}, followed by electron-beam deposition of 50 nm of Au deposited at 1.5 Å s^{-1} and finally 120 nm of thermally evaporated silver deposited at 3.0 Å s^{-1}.

Absorption and Scattering Measurements. UV−vis−NIR absorption and scattering spectra were taken in an integrating sphere for a drop-cast ensemble of nanorods or nanoshells on an ITO-coated glass substrate. Absorption curves were measured by tilting the sample at a slight angle relative to the illumination beam with all other ports closed so that all directly transmitted, reflected, and off-angle-scattered light was collected by the detector. Scattering curves were measured by orienting the sample normal to the incident beam with a port opposite the input port open so that only the off-angle-scattered light was detected. The 100% transmission baseline for both curves was measured with a bare ITO-coated glass substrate oriented at a slight angle relative to the illumination beam.

AM1.5 Photovoltaic Device Characterization. All photovoltaic and EQE device measurements were done under inert N_2-flow. Current−voltage measurements were done using a Keithley 2400 source meter with illumination from a solar simulator (Sciencetech, Class A, intensity = 100 mW cm^{-2}). The source intensity was measured with a Melles-Griot broadband power meter through a circular 0.049 cm^2 aperture. The spectral mismatch factor between the measured and actual solar spectrum was calculated to be 10%; thus a correction factor of 0.90 was applied to all current measurements. The uncertainty in the AM 1.5 characterization was estimated to be 7%.

External Quantum Efficiency Measurements. External quantum efficiency measurements were obtained by applying chopped (220 kHz) monochromatic illumination (400 W xenon lamp through a monochromator with order-sorting filters) collimated and cofocused with a 1 sun intensity white-light source on the device of interest. The power was measured with calibrated Newport 818-UV and Newport 818-IR power meters. The response from the chopped signal was measured using a Stanford Research Systems lock-in amplifier at short-circuit conditions. The uncertainty in the EQE measurements was estimated to be ±8%.

■ ASSOCIATED CONTENT

Ⓢ Supporting Information

Absorption and scattering measurements of nanorods and nanoshells, FDTD simulations for various nanoshell locations, electric field and absorption profiles, EDX line scan compositional analysis, and tabulated device data. This material is available free of charge via the Internet at http://pubs.acs.org.

AUTHOR INFORMATION

Corresponding Author

*E-mail: ted.sargent@utoronto.ca.

Author Contributions

D.P.S., A. Lee, S.M.T., and E.H.S. designed the study, analyzed the results, and wrote the manuscript. D.P.-S., A. Lee, and S.M.T. contributed to all experimental work. M.A. performed the FDTD simulations and analyzed the results. H.D. and M.Y. contributed to device fabrication. P.M. assisted with the absorption measurements. A. Labelle assisted with electron microscopy. S.H. and E.K. assisted with experiment design and analysis. K.L. carried out the nanorod synthesis. The manuscript was written through contributions of all authors. D.P.-S., A. Lee, and S.M.T. contributed equally.

Notes

The authors declare no competing financial interest.

ACKNOWLEDGMENTS

This publication is based in part on work supported by an award (KUS-11-009-21) from the King Abdullah University of Science and Technology (KAUST), by the Ontario Research Fund Research Excellence Program and by the Natural Sciences and Engineering Research Council (NSERC) of Canada. The authors thank I. Kramer, E. Palmiano, R. Wolowiec and D. Kopilovic for their help during the course of the study. H.D. would like to acknowledge financial support from China Scholarship Council (CSC).

REFERENCES

(1) Brown, M. D.; Suteewong, T.; Kumar, R. S. S.; Innocenzo, V. D.; Petrozza, A.; Lee, M. M.; Wiesner, U.; Snaith, H. J. *Nano Lett.* **2011**, *11*, 438−445.

(2) Hägglund, C.; Zäch, M.; Kasemo, B. *Appl. Phys. Lett.* **2008**, *92*, 013113.

(3) Thomann, I.; Pinaud, B. A.; Chen, Z.; Clemens, B. M.; Jaramillo, T. F.; Brongersma, M. L. *Nano Lett.* **2011**, *11*, 3440−3446.

(4) Rand, B. P.; Peumans, P.; Forrest, S. R. *J. Appl. Phys.* **2004**, *96*, 7519−7526.

(5) Yang, J.; You, J.; Chen, C.; Hsu, W.; Tan, H.; Zhang, X. W.; Hong, Z.; Yang, Y. *ACS Nano* **2011**, *5*, 6210−6217.

(6) Catchpole, K. R.; Polman, A. *Opt. Express* **2008**, *16*, 21793−800.

(7) Nakayama, K.; Tanabe, K.; Atwater, H. A. *Appl. Phys. Lett.* **2008**, *93*, 121904.

(8) Arquer, F. P. G. De; Beck, F. J.; Bernechea, M.; Konstantatos, G. *Appl. Phys. Lett.* **2012**, *100*, 043101.

(9) Ferry, V. E.; Verschuuren, M. A.; van Lare, M. C.; Schropp, R. E. I.; Atwater, H. A.; Polman, A. *Nano Lett.* **2011**, *11*, 4239−4245.

(10) Ding, I.-K.; Zhu, J.; Cai, W.; Moon, S.-J.; Cai, N.; Wang, P.; Zakeeruddin, S. M.; Grätzel, M.; Brongersma, M. L.; Cui, Y.; McGehee, M. D. *Adv. Energy Mater.* **2011**, *1*, 52−57.

(11) Li, X.; Choy, W. C. H.; Huo, L.; Xie, F.; Sha, W. E. I.; Ding, B.; Guo, X.; Li, Y.; Hou, J.; You, J.; Yang, Y. *Adv. Mater.* **2012**, *24*, 3046−52.

(12) Oulton, R. F.; Sorger, V. J.; Zentgraf, T.; Ma, R.-M.; Gladden, C.; Dai, L.; Bartal, G.; Zhang, X. *Nature* **2009**, *461*, 629−632.

(13) Okamoto, K.; Niki, I.; Shvartser, A.; Narukawa, Y.; Mukai, T.; Scherer, A. *Nat. Mater.* **2004**, *3*, 601−605.

(14) Knight, M.; Sobhani, H.; Nordlander, P.; Halas, N. *Science* **2011**, *332*, 702−704.

(15) Anker, J.; Hall, W.; Lyandres, O.; Shah, N. *Nat. Mater.* **2008**, *7*, 442−453.

(16) Atwater, H. A.; Polman, A. *Nature* **2010**, *9*, 205−213.

(17) Green, M.; Pillai, S. *Nat. Photonics* **2012**, *6*, 130−132.

(18) Pillai, S.; Beck, F. J.; Catchpole, K. R.; Ouyang, Z.; Green, M. A. *J. Appl. Phys.* **2011**, *109*, 73105.

(19) Arquer, F. P. G. De; Beck, F. J.; Konstantatos, G. *Opt. Express* **2011**, *19*, 21038−21049.

(20) Pala, R. A.; White, J.; Barnard, E.; Liu, J.; Brongersma, M. L. *Adv. Mater.* **2009**, *21*, 3504−3509.

(21) Salvador, M.; Macleod, B. A.; Hess, A.; Kulkarni, A. P.; Munechika, K.; Chen, J. I. L.; Ginger, D. S.; Al, S. E. T. *ACS Nano* **2012**, *6*, 10024−10032.

(22) Quinten, M. *Appl. Phys. B: Laser Opt.* **2001**, *73*, 245−255.

(23) Sönnichsen, C.; Reinhard, B. M.; Liphardt, J.; Alivisatos, A. P. *Nat. Biotechnol.* **2005**, *23*, 741−5.

(24) Pillai, S.; Green, M. A. *Sol. Energy Mater. Sol. Cells* **2010**, *94*, 1481−1486.

(25) Huang, X.; Neretina, S.; El-Sayed, M. A. *Adv. Mater.* **2009**, *21*, 4880−4910.

(26) Lee, A.; Andrade, G. F. S.; Ahmed, A.; Souza, M. L.; Coombs, N.; Tumarkin, E.; Liu, K.; Gordon, R.; Brolo, A. G.; Kumacheva, E. *J. Am. Chem. Soc.* **2011**, *133*, 7563−70.

(27) Aizpurua, J.; Bryant, G. W.; Richter, L. J.; García de Abajo, F. J. *Phys. Rev. B* **2005**, *71*, 235420.

(28) Link, S.; Mohamed, M. B.; El-Sayed, M. A. *J. Phys. Chem. B* **1999**, *103*, 3073−3077.

(29) Oldenburg, S.; Averitt, R.; Westcott, S.; Halas, N. *Chem. Phys. Lett.* **1998**, *288*, 243−247.

(30) Bardhan, R.; Grady, N. K.; Cole, J. R.; Joshi, A.; Halas, N. J. *ACS Nano* **2009**, *3*, 744−752.

(31) Ip, A. H.; Thon, S. M.; Hoogland, S.; Voznyy, O.; Zhitomirsky, D.; Debnath, R.; Levina, L.; Rollny, L. R.; Carey, G. H.; Fischer, A.; Kemp, K. W.; Kramer, I. J.; Ning, Z.; Labelle, A. J.; Chou, K. W.; Amassian, A.; Sargent, E. H. *Nat. Nanotechnol.* **2012**, *7*, 577−82.

(32) Kramer, I. J.; Zhitomirsky, D.; Bass, J. D.; Rice, P. M.; Topuria, T.; Krupp, L.; Thon, S. M.; Ip, A. H.; Debnath, R.; Kim, H.-C.; Sargent, E. H. *Adv. Mater.* **2012**, *24*, 2315−9.

(33) Scharber, M. C.; Mühlbacher, D.; Koppe, M.; Denk, P.; Waldauf, C.; Heeger, A. J.; Brabec, C. J. *Adv. Mater.* **2006**, *18*, 789−794.

(34) Prodan, E.; Radloff, C.; Halas, N. J.; Nordlander, P. *Science* **2003**, *302*, 419−22.

(35) Prodan, E.; Nordlander, P.; Halas, N. J. *Nano Lett.* **2003**, *3*, 1411−1415.

(36) Pattantyus-Abraham, A. G.; Kramer, I. J.; Barkhouse, A. R.; Wang, X.; Konstantatos, G.; Debnath, R.; Levina, L.; Raabe, I.; Nazeeruddin, M. K.; Sargent, E. H. *ACS Nano* **2010**, *4*, 3374−3380.

(37) Ross, B. M.; Tasoglu, S.; Lee, L. P. *Proc. SPIE* **2009**, *7394*, 739422.

(38) Hines, M. A.; Scholes, G. D. *Adv. Mater.* **2003**, *15*, 1844−1849.

(39) Nikoobakht, B.; El-Sayed, M. *Chem. Mater.* **2003**, *15*, 1957−1962.